Magnetic skyrmion Walker breakdown in cylindrical nanotubes

Weiwei Wang,[1] Pengfei Hu,[1] Lingyao Kong,[2,*] Dongsheng Song,[1] and Haifeng Du[3]
[1]*Institutes of Physical Science and Information Technology, Anhui University, Hefei 230601, China*
[2]*School of Physics and Optoelectronic Engineering, Anhui University, Hefei 230601, China*
[3]*Anhui Key Laboratory of Condensed Matter Physics at Extreme Conditions, High Magnetic Field Laboratory, HFIPS, Anhui, Chinese Academy of Sciences, Hefei 230031, China*

(Received 25 January 2023; accepted 24 March 2023; published 7 April 2023)

As topological spin textures, magnetic skyrmions in chiral magnets show a universal current-velocity relation when driven by spin transfer torques. In general, the skyrmions in chiral magnets do not exhibit Walker breakdown—a phenomenon that domain walls' motion modes will change from steady to precessional motion when the driving forces are sufficiently large. In this work, we studied the dynamics of magnetic skyrmions in cylindrical nanotubes numerically and analytically. The skyrmion performs a helical motion in the nanotube without external fields. However, we show that the skyrmion exhibits the Walker breakdown phenomenon when an external field is applied to the nanotube perpendicularly. A steady skyrmion motion is observed in the low current regime, while the skyrmion moves forward and back when the current is larger than a critical density. Our findings reveal a new way to tune the skyrmion dynamics beyond planar geometries.

DOI: 10.1103/PhysRevB.107.134407

I. INTRODUCTION

Walker breakdown [1] is a well known phenomenon that the domain walls' motion modes will change from steady to precessional motion when the driving forces are more significant than a threshold, accompanying a sudden drop in the propagation velocity [2]. The Walker breakdown of domain wall has been observed in ferromagnets [1], ferrimagnets [3], antiferromagnets [4,5], and multilayered systems [6,7] for various driving forces such as the external fields [1], spin transfer torques [2], and spin-orbit torques [8]. As an emergent phenomenon, the Walker breakdown does not typically occur in narrow cylindrical nanowires because a nanowire can be simplified as a uniaxial anisotropy system [9]. Therefore, a minimal model to reproduce the Walker breakdown phenomenon is a ferromagnetic system with two effective anisotropies, for instance, a Permalloy nanostrip in which the two anisotropies originate from demagnetization. In such a system, one anisotropy stabilizes the domain wall, and the other forms a potential that limits the precessional motion in the low driving force regime. It thus shows a steady motion, as shown in Fig. 1(a). As the driving forces (such as current density j or external fields) increase, the potential fails to suppress the precessional motion, resulting in a drop in velocity.

Like domain walls, the magnetic skyrmions [10,11] are topological solitons with particlelike properties [12]. The domain walls and skyrmions are considered promising candidates for spintronic applications [13–16]. The magnetic skyrmions show fascinating dynamics in nonequilibrium environments. For example, a skyrmion moves towards the high-temperature region in the presence of temperature gradients [17,18], whereas an interstitial skyrmion will move from the hot area to the cold area [19]. However, the skyrmion dynamics driven by currents are pretty simple–it shows a universal current-velocity relation [20,21]. Therefore, the Walker breakdown of magnetic skyrmions in chiral magnets has not been observed.

In this work, we investigate the dynamics of a magnetic skyrmion in cylindrical nanotubes driven by spin transfer torques. We show that Walker breakdown of magnetic skyrmion emerges when an external field perpendicular to the cylindrical nanotubes is applied.

II. MODEL

The cylindrical nanotubes are curved shapes. In this situation, a common approach is to use the finite element method to discretize the (continuum) micromagnetic energy [22,23]. Instead of using classical micromagnetic simulations [24,25], we follow the idea of mapping the micromagnetic energy into the classical Heisenberg model on a regular cylindrical mesh [26], which is valid as long as the tube radius is much larger than the thickness of the tube. A typical cylindrical mesh along the z axis is shown in Fig. 1(b). Based on the cylindrical mesh, we consider the nearest-neighbor exchange interaction, the bulk-type DMI, a uniaxial anisotropy, and an external field perpendicular to the tube. Accordingly, the system's Hamiltonian can be written as

$$\mathcal{H} = -J\sum_{\langle i,j\rangle}\mathbf{m}_i\cdot\mathbf{m}_j + \sum_{\langle i,j\rangle}\mathbf{D}_{ij}\cdot[\mathbf{m}_i\times\mathbf{m}_j] - \sum_i K(\mathbf{e}_r\cdot\mathbf{m}_i)^2 - \sum_i \mu_s\mathbf{m}_i\cdot\mathbf{H}, \quad (1)$$

where $\langle i, j\rangle$ represents a unique pair of lattice sites i and j, $\mathbf{m}_i$ is the unit vector of the magnetic moment $\boldsymbol{\mu}_i = -\hbar\gamma\mathbf{S}_i$ with $\mathbf{S}_i$ being the atomistic spin, and $\gamma(>0)$ the gyromagnetic ratio. The bulk-type DMI vector $\mathbf{D}_{ij}$ can be written as $\mathbf{D}_{ij} = D\hat{\mathbf{r}}_{ij}$,

*LyKong@ahu.edu.cn

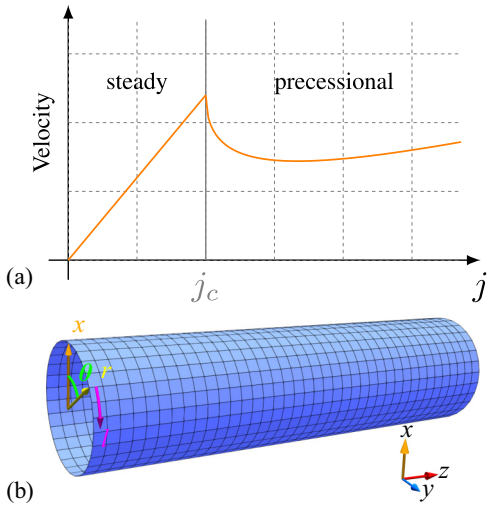

FIG. 1. (a) Schematic illustration of Walker breakdown of magnetic domain walls where j represents the current density. The domain wall shows a steady motion in the low current regime and changes to the precessional mode when the current density is larger than the critical density, accompanying the velocity dropdown. (b) A regular cylindrical mesh with $n_z = 40$ and $n_l = 30$ where n_z and n_l are the number of nodes along the z and tangential direction. The lattice spacing along the z axis is a, and the radius $R = 5a$. Spins are located in each mesh site, and θ is the angle between $\mathbf{e}_x$ and $\mathbf{e}_r$.

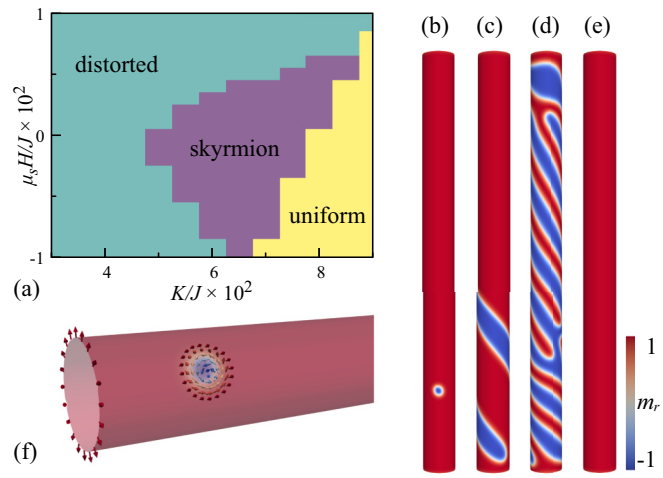

FIG. 2. (a) The phase diagram in the cylindrical nanotube as a function of H and K. The phase diagram is obtained by minimizing the system energy starting from the skyrmion state. Possible states are (b) isolated skyrmion, (c) stretched skyrmion, (d) multidomain state, and (e) uniform domain. The isolated skyrmion with skyrmion number $Q = -1$ is emphasized in (f). A coolwarm colormap is used for plotting m_r.

where D is the DMI constant and $\hat{\mathbf{r}}_{ij}$ is the unit vector between $\mathbf{S}_i$ and $\mathbf{S}_j$. The anisotropy $K(>0)$ denotes the easy-uniaxial anisotropy along the radial direction and the external field is applied in the x direction, i.e., $\mathbf{H} = H\mathbf{e}_x$. The dipolar interaction has not been included in Eq. (1) explicitly since it can be cast into the local anisotropy K for thin shells [26].

We consider a FeGe cylindrical nanotube with a radius $R = 40$ nm and thickness of 2 nm. To describe the nanotube, we use a cylindrical mesh with $n_l = 128$ and $R = 20a$ with $a = 2$ nm. The cell size along the azimuthal direction is $\Delta l = 2\pi R/n_l = 1.96$ nm, which is close to $a = 2$ nm. The typical parameters of FeGe are used [24]: the saturation magnetization $M_s = 3.84 \times 10^5$A/m, the exchange constant $A = 8.78 \times 10^{-12}$J/m, the DMI strength D is determined by $L = 4\pi A/D$ with helix period $L = 70$ nm. Therefore, we obtain the simulation parameters $J = 2Aa$, $D/J = 2\pi a/L \approx 0.18$, $\mu_s = M_s a^3$. We have used JuMag [27] to perform the simulations.

Similar to the planar system, a magnetic skyrmion can be stabilized in a nanotube using external fields or anisotropy. Fig. 2(a) shows the phase diagram with various external fields (H) and anisotropy (K), which is obtained by minimizing the system energy that starts from the skyrmion state at $\theta = \pi$. The isolated skyrmion can be stabilized by the anisotropy alone, as shown in Fig. 2(b), where $K/J = 0.06$ is used. The diameter of the skyrmion is close to the helix period 70 nm. The skyrmion number is $Q = -1$, which is defined as

$$Q = \frac{1}{4\pi}\int \mathbf{m}\cdot\left(\frac{\partial \mathbf{m}}{\partial l}\times\frac{\partial \mathbf{m}}{\partial z}\right)\mathrm{d}l\mathrm{d}z, \tag{2}$$

where $l = R\theta$. Moreover, the skyrmion is tilted due to the curvature of the nanotube [25,28]. For a specific skyrmion in the nanotube, the stabilized region of the external field is not symmetric. In the low anisotropy region, the distorted states such as stretched skyrmion [25] [Fig. 2(c)] or multidomain state [Fig. 2(d)] may be formed. As the strength of anisotropy increases, the background becomes a radical state [Fig. 2(e)], which corresponds to the ferromagnetic state in the planar system.

In the presence of currents, the magnetization dynamics is govenered by the extended Landau-Lifshitz-Gilbert (LLG) equation with spin transfer torques, which reads [29,30]

$$\begin{aligned}\frac{\partial \mathbf{m}}{\partial t} =& -\gamma \mathbf{m}\times\mathbf{H}_{\text{eff}} + \alpha\mathbf{m}\times\frac{\partial \mathbf{m}}{\partial t}\\ &-(\mathbf{u}\cdot\nabla)\mathbf{m} + \beta[\mathbf{m}\times(\mathbf{u}\cdot\nabla)\mathbf{m}],\end{aligned} \tag{3}$$

where $\mathbf{m}$ is the unit vector of the magnetization, $\mathbf{H}_{\text{eff}} = -\frac{1}{\mu_s}\frac{\partial \mathcal{H}}{\partial \mathbf{m}_i}$ is the total effective field, α is the Gilbert damping, and β represents the strength of nonadiabatic spin transfer torques. The parameter $\mathbf{u}$ is defined as

$$\mathbf{u} = -\frac{gP\mu_B}{2eM_s}\mathbf{j} = -\frac{Pa^3}{2eS}\mathbf{j}, \tag{4}$$

where g is the Landé factor, μ_B is the Bohr magneton, $e(>0)$ is the electron charge, M_s is the saturation magnetization, P is the polarization rate of the current, S is the amplitude of atomistic spin, and $\mathbf{j}$ is the current density. We have used $P = 0.5$ in this work.

III. RESULTS

We first consider the skyrmion dynamics without the external fields, i.e., $H = 0$. The skyrmion moves towards the $+z$ direction under a current $u = 8$ m/s, as illustrated in Fig. 3(a). Meanwhile, the skyrmion rotates clockwise due to the skyrmion Hall effect, forming a helical trajectory. The corresponding skyrmion displacements are shown in Fig. 3(b),

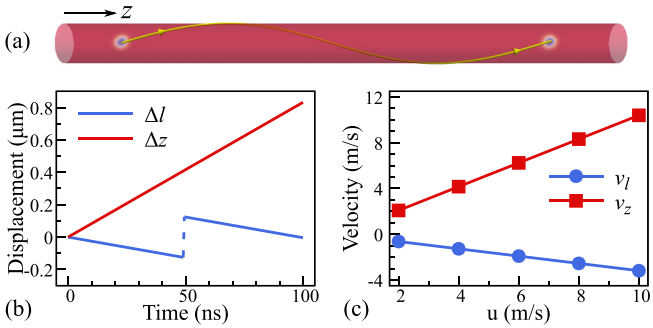

FIG. 3. (a) A skyrmion moves towards the $+z$ direction when a current $u = 8$ m/s is applied. Its trajectory shows a helical motion due to the skyrmion Hall effect. (b) The corresponding displacements of the skyrmion as a function of time. (c) The skyrmion velocity as a function of applied current u. The parameters $\alpha = 0.05$ and $\beta = 0.3$ are used.

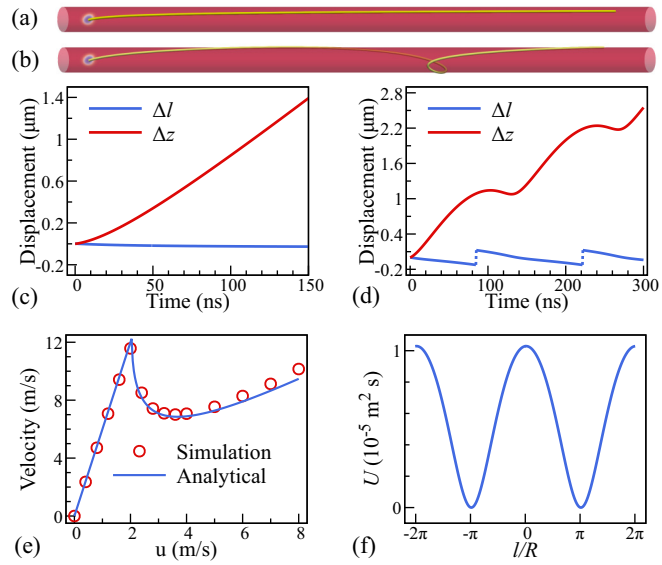

FIG. 4. The skyrmion dynamics in the presence of a perpendicular external field. (a) A steady skyrmion motion is observed when a current $u = 2$ m/s is applied. (b) The skyrmion moves forward and back when the current is increased to $u = 6$ m/s, indicating the applied current is in the Walker breakdown regime. The corresponding displacements of the skyrmion as a function of time for (c) $u = 2$ m/s and (d) $u = 6$ m/s. (e) The calculated skyrmion velocity v_z as a function of u. For $u > 2$ m/s, the average velocity $\langle v_z \rangle$ is used. The analytical velocities are plotted using blue lines. (f) The extracted potential of the skyrmion from the simulation.

where parameters $\alpha = 0.05$ and $\beta = 0.3$ are used because a large ratio of β/α is reported [31]. The z and l components change linearly under the current, which is the same as that in the planar films [20]. The trajectories are calculated using the guiding center (l^*, z^*), which is defined as $l^* = \int lqdzdl / \int qdzdl$ and $z^* = \int zqdzdl / \int qdzdl$, where $q = \mathbf{m} \cdot (\partial_l \mathbf{m} \times \partial_z \mathbf{m})$ is topological charge density. The skyrmion velocity as a function of current density is shown in Fig. 3(c). A simple linear relationship is observed, the same as the planar film scenario.

The dynamics of skyrmion motion in the nanotube can be understood using the collective coordinate approach [32]. Assuming that the skyrmion is rigid, only two degrees of freedom, i.e., the skyrmion position (l^*, z^*), are used to describe the skyrmion dynamics. In this situation, one obtains the Thiele equation

$$\mathbf{G} \times (\mathbf{v} - \mathbf{u}) + \mathcal{D}(\alpha \mathbf{v} - \beta \mathbf{u}) = \mathbf{F}, \tag{5}$$

where $\mathbf{v} = (v_l, v_z)$ is the skyrmion velocity, and $\mathbf{G} = G\mathbf{e}_r$ with $G = 4\pi Q$ describes the Magnus force. The second term denotes the dissipative force with the tensor $\mathcal{D}_{ij} = 4\pi \eta_{ij}$ associated with the shape factor and $\eta_{ij} = (1/4\pi) \int (\partial_i \mathbf{m} \cdot \partial_j \mathbf{m}) dl dz$. For a standard skyrmion without distortion, $\eta_{ij} = \delta_{ij}\eta$ and η is close to unity. The force F is directly related to the external field, which is given by $F_i = \int \gamma \mathbf{m} \cdot [\partial_i \mathbf{m} \times (\mathbf{m} \times \mathbf{H})] dz\, dl = \int \gamma \partial_i \mathbf{m} \cdot \mathbf{H}\, dz dl$. For the situation that $H = 0$ and current applied in the z direction, i.e., $\mathbf{u} = u\mathbf{e}_z$, the Thiele equation gives

$$v_z = \frac{1 + \eta^2 \alpha\beta}{1 + \alpha^2 \eta^2} u, \quad v_l = \frac{(\alpha - \beta)\eta}{1 + \alpha^2 \eta^2} u, \tag{6}$$

where $\mathbf{F} = \mathbf{0}$ and $Q = -1$ are used. Clearly, both v_z and v_l scale linearly with u, agreeing with the numerical results shown in Fig. 3(c). The clockwise motion is related to v_l, which depends on $\alpha - \beta$ and the skyrmion number Q.

We then study the skyrmion dynamics in the presence of perpendicular external fields, i.e., $\mu_s H/J = 0.003$. The skyrmion trajectories for $u = 2$ m/s and $u = 6$ m/s are shown in Fig. 4(a) and Fig. 4(b), respectively. For the current density $u = 2$ m/s, the second half of the skyrmion trajectory is simply a straight line. The z component of the skyrmion position has an acceleration process in the first stage (<50 ns) and eventually reaches a steady motion, as shown in Fig. 4(c). Meanwhile, the l component of the skyrmion position ultimately arrives at a saturated value.

However, for the current $u = 6$ m/s, the skyrmion shows a distorted helical trajectory. The displacement of the skyrmion quickly increases to 1143 nm at $t = 103$ ns, then decreases to 1077 nm at $t = 130$ ns. Meanwhile, its l component goes back to the initial position. This motion pattern repeats as time continues, corresponding to the precessional motion for the magnetic domain wall. The calculated velocity as a function of current density is shown in Fig. 4(d). The skyrmion velocity shows a sudden drop around $u = 2$ m/s, indicating the Walker Breakdown of magnetic skyrmions.

We return to the Thiele equation to understand the observed Walker breakdown phenomenon. The force $\mathbf{F}$ can be defined as $\mathbf{F} = -\nabla U$ where $U = U(l, z)$ is a potential that acts on the skyrmion. Considering the translating symmetry, we have $F_z = 0$ and $F_l = -\partial_l U(l)$. The potential originates from the Zeeman energy. However, we use the total micromagnetic energy E to compute the potential because the skyrmion size varies in different positions. The calculated potential using $U = \gamma E/(\mu_0 M_s t_0)$ is shown in Fig. 4(f), where t_0 is the tube thickness. As expected, it is not a standard sinusoidal function.

As an approximation, we ignore the changes in skyrmion size and use a sinusoidal potential $U(l) = U_0[1 + \cos(l/R)]$, we arrive at

$$v_l = u_1 + U_1 \sin(l/R) \tag{7}$$

$$v_z = \frac{\beta}{\alpha}u + \frac{1}{\alpha\eta}v_l \tag{8}$$

where $U_1 = (1/4\pi R)\alpha\eta U_0/(1+\alpha^2\eta^2)$ and $u_1 = (\alpha - \beta)\eta/(1+\alpha^2\eta^2)u$. For a low current density $u < u_c$, the skyrmion can not move freely in the tangential direction due to the potential U. In this situation, the solution of Eq. (7) is $v_l = 0$ and

$$v_z = \frac{\beta}{\alpha}u. \tag{9}$$

The critical current density u_c is given by

$$u_c = \frac{\alpha U_0}{4\pi R|\alpha - \beta|}. \tag{10}$$

From Fig. 4(f), the parameter U_0 is established as $U_0 = 5.15 \times 10^{-6}\mathrm{m}^2\cdot$ s, which gives $u_c = 2.05$ m/s. For a high current density $u > u_c$, the solution of Eq. (7) is

$$u_1 \tan\left(\frac{l}{2R}\right) + U_1 = B\tan\left(\frac{Bt}{2R} - c\right), \tag{11}$$

where $B = \sqrt{u_1^2 - U_1^2} = [|\alpha - \beta|\eta/(1+\alpha^2\eta^2)]\sqrt{u^2 - u_c^2}$ and c is a constant. The period is $T = 2R\pi/B$ and thus the average velocity is computed as $\langle v_l\rangle = \Delta l/T = \mathrm{sgn}(u_1)B = [(\alpha - \beta)\eta/(1+\alpha^2\eta^2)]\sqrt{u^2 - u_c^2}$. Therefore, the average velocity of the skyrmion for $u > u_c$ can be established as

$$\langle v_z\rangle = \frac{\beta}{\alpha}u + \frac{\sqrt{u^2 - u_c^2}}{1+\alpha^2\eta^2}\left(1 - \frac{\beta}{\alpha}\right). \tag{12}$$

The analytical velocities [Eqs. (9) and (12)] are plotted in Fig. 4(f) using blue lines, where $\eta = 1.2$ is used. It is found that the analytical velocities agree with the simulation results well.

IV. SUMMARY

In summary, we have studied the skyrmion dynamics driven by currents in a cylindrical nanotube. Without the external fields, the skyrmion shows a helical motion in the nanotube. A steady skyrmion motion is observed under a low current density in the presence of a perpendicular external field. As the current density increases, the skyrmion moves forward and back, indicating the Walker breakdown motion pattern. Our work reveals a new way to tune the skyrmion dynamics beyond planar geometries. Moreover, the observed skyrmion Walker breakdown may occur in other magnetic systems, such as cylindrical multilayers driven with Slonczewski spin transfer torques.

ACKNOWLEDGMENTS

We acknowledges financial support from the National Key R&D Program of China (Grant No. 2022YFA1403603) and the Strategic Priority Research Program of Chinese Academy of Sciences (Grant No. XDB33030100), the National Natural Science Foundation of China (Grants No. 52173215, No. 11974021, and No. 12241406), the Natural Science Foundation of Anhui Province for Excellent Young Scientist (Grant No. 2108085Y03) and the National Natural Science Fund for Excellent Young Scientists Fund Program (Overseas).

[1] N. L. Schryer and L. R. Walker, J. Appl. Phys. **45**, 5406 (1974).
[2] A. Mougin, M. Cormier, J. P. Adam, P. J. Metaxas, and J. Ferré, Europhys. Lett. **78**, 57007 (2007).
[3] J. Hütner, T. Herranen, and L. Laurson, Phys. Rev. B **99**, 174427 (2019).
[4] K. Pan, L. Xing, H. Y. Yuan, and W. Wang, Phys. Rev. B **97**, 184418 (2018).
[5] R. M. Otxoa, P. E. Roy, R. Rama-Eiroa, J. Godinho, K. Y. Guslienko, and J. Wunderlich, Commun. Phys. **3**, 190 (2020).
[6] I. Lemesh and G. S. D. Beach, Phys. Rev. Appl. **12**, 044031 (2019).
[7] J. Moon, J. Yoon, K. Kim, S.-H. Lee, D.-Y. Kim, and S.-B. Choe, Sci. Rep. **12**, 2307 (2022).
[8] P.-B. He, M.-Q. Cai, and Z.-D. Li, Phys. Rev. B **102**, 224419 (2020).
[9] M. Yan, A. Kákay, S. Gliga, and R. Hertel, Phys. Rev. Lett. **104**, 057201 (2010).
[10] S. Mühlbauer, B. Binz, F. Jonietz, C. Pfleiderer, A. Rosch, A. Neubauer, R. Georgii, and P. Böni, Science **323**, 915 (2009).
[11] X. Z. Yu, Y. Onose, N. Kanazawa, J. H. Park, J. H. Han, Y. Matsui, N. Nagaosa, and Y. Tokura, Nature (London) **465**, 901 (2010).
[12] N. Nagaosa and Y. Tokura, Nat. Nanotechnol. **8**, 899 (2013).
[13] A. Fert, V. Cros, and J. Sampaio, Nat. Nanotechnol. **8**, 152 (2013).
[14] K. M. Song, J.-S. Jeong, B. Pan, X. Zhang, J. Xia, S. Cha, T.-E. Park, K. Kim, S. Finizio, J. Raabe, J. Chang, Y. Zhou, W. Zhao, W. Kang, H. Ju, and S. Woo, Nature Electronics **3**, 148 (2020).
[15] P. Barla, V. K. Joshi, and S. Bhat, J. Comput. Electron. **20**, 805 (2021).
[16] J. Tang, Y. Wu, W. Wang, L. Kong, B. Lv, W. Wei, J. Zang, M. Tian, and H. Du, Nat. Nanotechnol. **16**, 1086 (2021).
[17] L. Kong and J. Zang, Phys. Rev. Lett. **111**, 067203 (2013).
[18] M. Weißenhofer, L. Rózsa, and U. Nowak, Phys. Rev. Lett. **127**, 047203 (2021).
[19] L. Kong, X. Chen, W. Wang, D. Song, and H. Du, Phys. Rev. B **104**, 214407 (2021).
[20] J. Iwasaki, M. Mochizuki, and N. Nagaosa, Nat. Commun. **4**, 1463 (2013).
[21] W. Wang, D. Song, W. Wei, P. Nan, S. Zhang, B. Ge, M. Tian, J. Zang, and H. Du, Nat. Commun. **13**, 1593 (2022).
[22] M. Yan, C. Andreas, A. Kákay, F. García-Sánchez, and R. Hertel, Appl. Phys. Lett. **99**, 122505 (2011).
[23] J. Yang, J. Kim, C. Abert, D. Suess, and S.-K. Kim, Phys. Rev. B **102**, 094439 (2020).
[24] M. Xin and Y. Liu, J. Magn. Magn. Mater. **536**, 168142 (2021).
[25] X. Wang, X. S. Wang, C. Wang, H. Yang, Y. Cao, and P. Yan, J. Phys. D **52**, 225001 (2019).
[26] D. Kechrakos, L. Tzannetou, and A. Patsopoulos, Phys. Rev. B **102**, 054439 (2020).

[27] JuMag–A Julia package for classical spin dynamics and micromagnetic simulations with GPU support, https://github.com/ww1g11/JuMag.jl.
[28] X. Huo and Y. Liu, New J. Phys. **21**, 093024 (2019).
[29] S. Zhang and Z. Li, Phys. Rev. Lett. **93**, 127204 (2004).
[30] A. Thiaville, Y. Nakatani, J. Miltat, and Y. Suzuki, Europhys. Lett. **69**, 990 (2005).
[31] D. Song, W. Wang, J.-X. Yu, P. Zhang, S. S. Pershoguba, G. Yin, W. Wei, J. Jiang, B. Ge, X. Fan, M. Tian, A. Rosch, J. Zang, and H. Du, arXiv:2212.08991 [cond-mat, physics:physics].
[32] O. A. Tretiakov, D. Clarke, G.-W. Chern, Y. B. Bazaliy, and O. Tchernyshyov, Phys. Rev. Lett. **100**, 127204 (2008).